SUPPLEMENTARY INFORMATION

Mechanism for DPY30 and ASH2L Intrinsically Disordered Regions to Modulate MLL/SET1 Activity on Chromatin

Young-Tae Lee, Alex Ayoub, Sang-Ho Park, Liang Sha, Jing Xu, Fengbiao Mao, Wei Zheng, Yang Zhang, Uhn-Soo Cho, and Yali Dou

SUPPLEMENTARY FIGURES

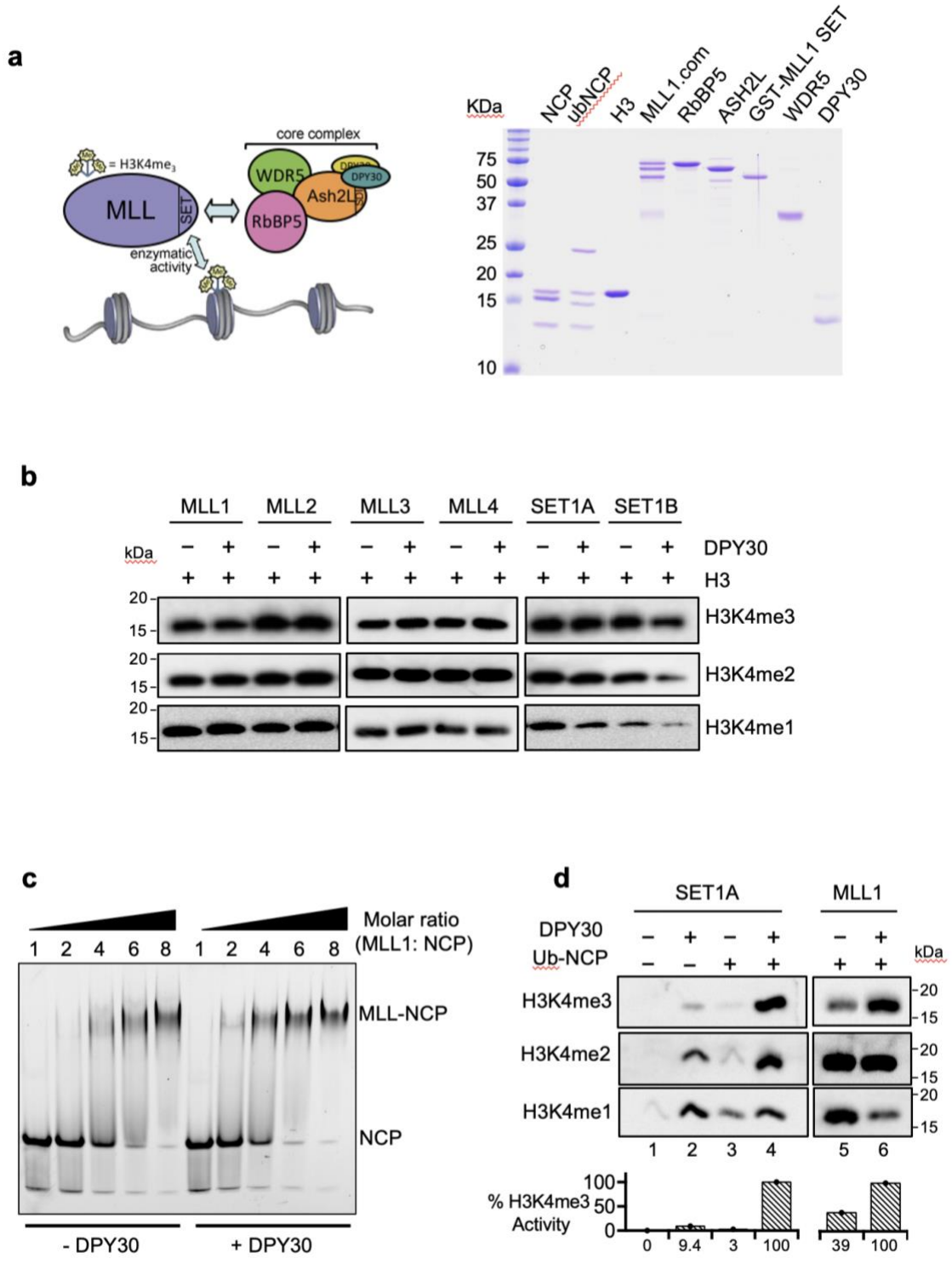

Supplementary Figure 1 | DPY30 stimulates MLL1/SET1 activity on the NCP. This figure is related to main Figure 1. **a**, Left, cartoon model of the subunits that comprise the MLL core complex. Full-length components are represented here and used in experiments with the exception of MLL1 protein, where only the SET is used in the HMT assay. Right, Coomassie

brilliant blue staining of recombinant proteins used in this study including the NCP, the H2BK120ub-containing NCP, recombinant histone H3, the MLL1 core complex and individual components of the MLL1 core complex as indicated on top. **b**, DPY30 does not affect MLL1 activity on recombinant H3. *In vitro* HMT assay for the MLL/SET1 family histone methyltransferases using recombinant H3 as the substrate. The reactions were carried out for longer time than those on the NCP and the immunoblots were subject to a longer exposure due to weaker enzymatic activity of these enzymes on recombinant histone H3. Antibodies used for immunoblots were indicated on right. **c**, DPY30 does not affect binding of the MLL1 complex to the NCP. Electrophoretic mobility shift assay of the MLL1 core complex binding to nucleosome in the presence or absence of DPY30. Molar ratio of the MLL1 complex to NCP was indicated on top. NCP concentration was 0.4 μM. **d**, DPY30 and H2BK120ub stimulate SET1 and MLL1 activity through distinct mechanisms. *In vitro* HMT assay for the SET1A and the MLL1 core complexes on unmodified NCP (denoted as '-') or H2BK120ub-NCP ('+') substrates as indicated on top. Quantification of H3K4me3 was done using ImageJ [1] and presented as relative %activity to that of lane 4 and lane 6, respectively.

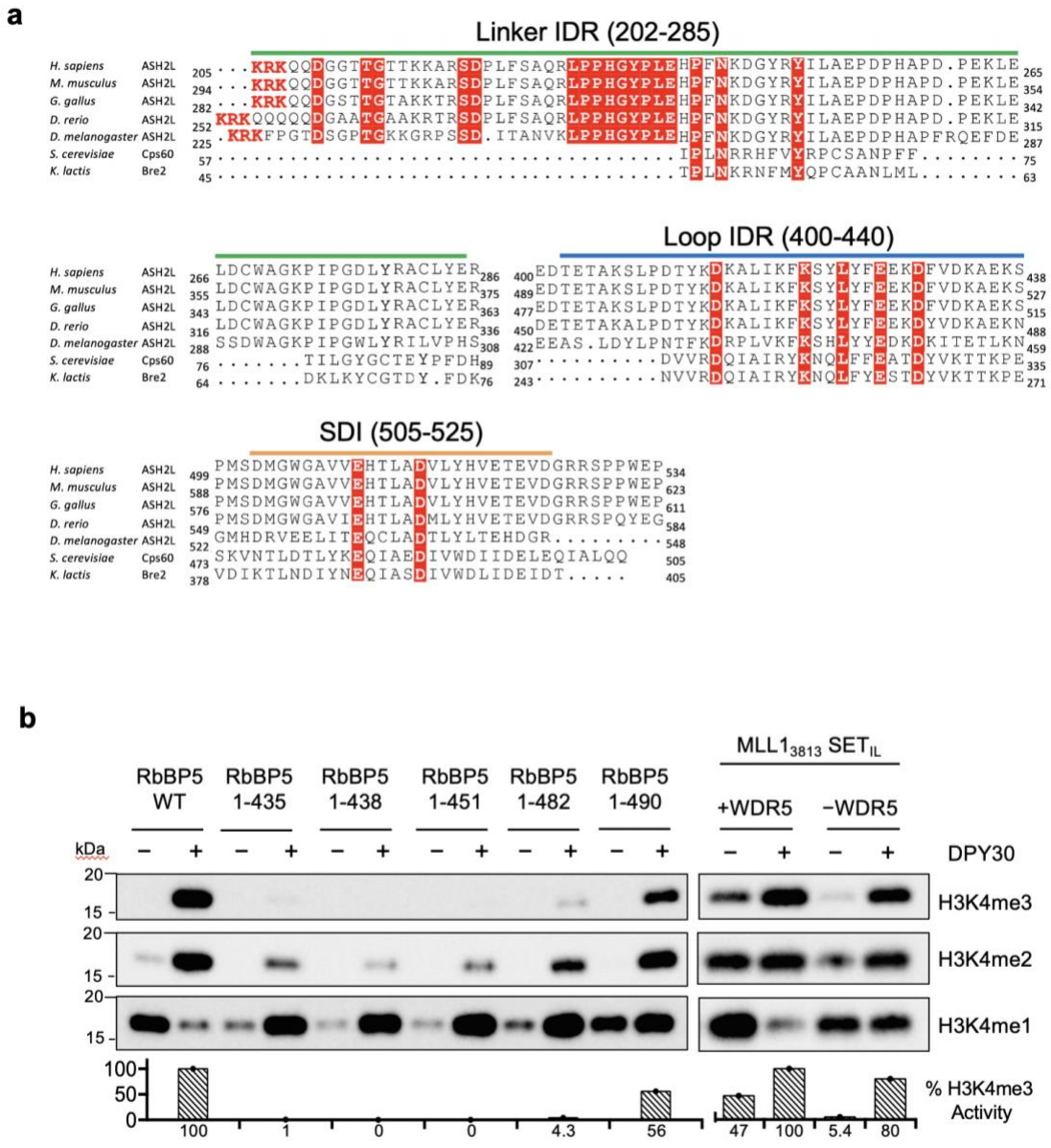

Supplementary Figure 2 | IDRs in RbBP5 and MLL1^{SET} are not essential for DPY30-dependent regulation. This figure is related to main Figure 2 and Figure 3. **a**, Sequence alignment for eukaryotic ASH2L and ASH2L homologs. Highly conserved sequences are highlighted in red. IDR regions of interest (i.e., Linker, Loop, and SDI) are annotated. **b**, *In vitro* HMT assay for the MLL1 complex containing RbBP5 truncation fragments (left) or the MLL13813$^{SET\ N3861I/Q3867L}$ (MLL^{SETIL}) with or without WDR5 (right) as indicated on top. RbBP5 has an N-terminal WD40 repeat (1-381aa) and a C-terminal IDR (382-538aa). We serially deleted RbBP5 from C-terminus to gradually removed C-terminal IDRs. The assays were performed in the presence or absence of DPY30. Antibodies used in the immunoblots were indicated on right. Quantification of H3K4me3 for reaction containing DPY30 was done using ImageJ [1] and presented as relative %activity to that of MLL1 complex with wild type RbBP5.

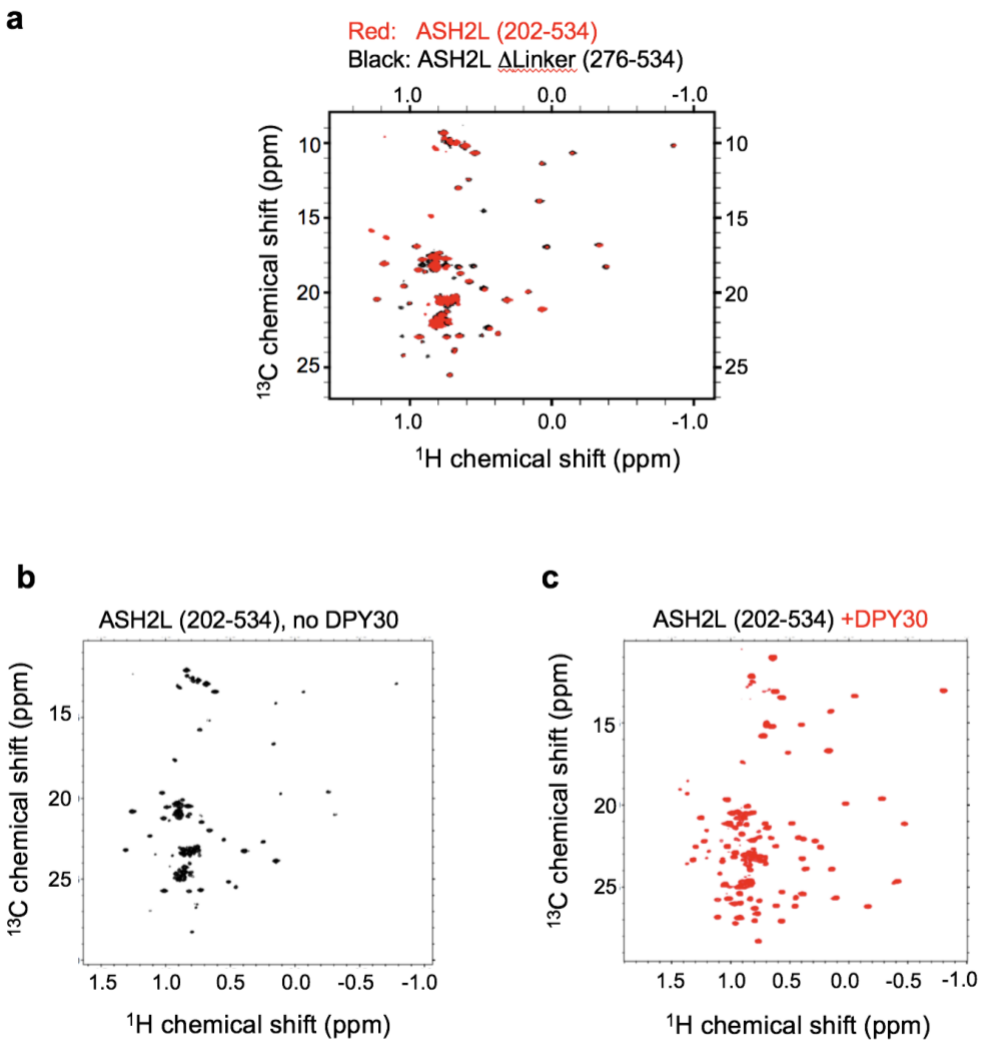

Supplementary Figure 3 | NMR spectra for ASH2L. This figure is related to main Figure 4a. **a**, Linker IDR does not have NMR spectra in the apo-state of full length ASH2L. Methyl-TROSY spectra of [^{2}H, $^{13}CH_3$-ILV] ASH2L$^{202-534}$ (red) and [^{2}H, $^{13}CH_3$-ILV] ASH2L$^{\Delta Linker,276-534}$ (black) were superimposed. **b-c**, ASH2L spectra undergo drastic changes upon addition of DPY30. **b**, Methyl-TROSY spectrum of [^{2}H, $^{13}CH_3$-ILV] ASH2L$^{202-534}$ in the absence of DPY30. **c**, Methyl-TROSY spectrum of [^{2}H, $^{13}CH_3$-ILV] ASH2L$^{202-534}$ in complex with DPY30. Stoichiometric ratio between ASH2L and homodimeric DPY30 was 1:1.2.

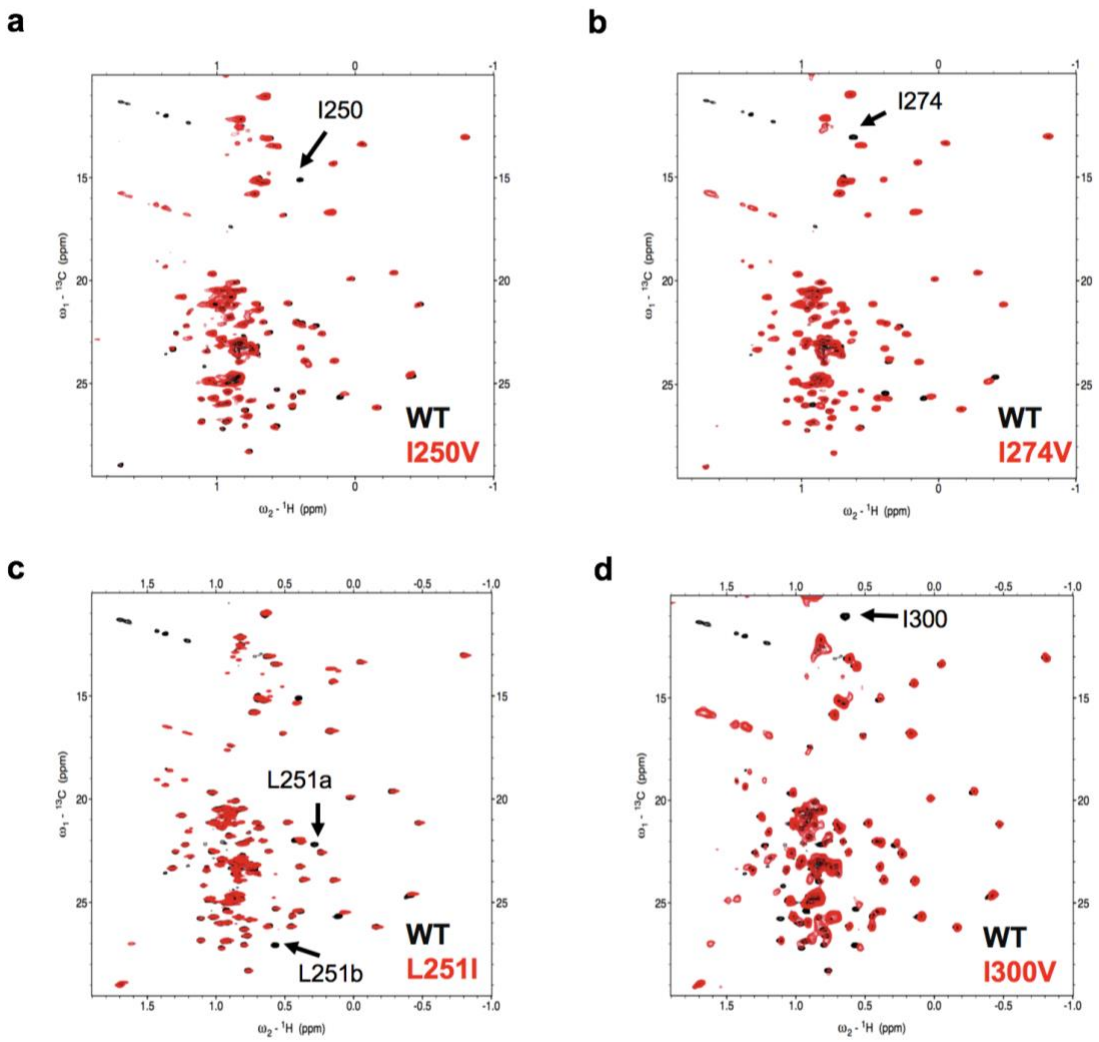

Supplementary Figure 4 | Examples for the residue-specific mutagenesis assignment by methyl-TROSY approach. This figure is related to main Figure 4a. **a**, Superimposed methyl-TROSY spectra of DPY30-bound [^{2}H, $^{13}CH_3$-ILV] wild-type ASH2L$^{202-534}$ (black) and single residue mutant ASH2L$^{202-534,\ I250V}$ constructs (red). Disappeared peak was assigned to the mutated residue. **b**, I274V, **c**, L251I and **d**, I300V were examined for residue-specific mutagenesis assignment by methyl-TROSY. Using this approach, 65% of peaks were assigned without ambiguity.

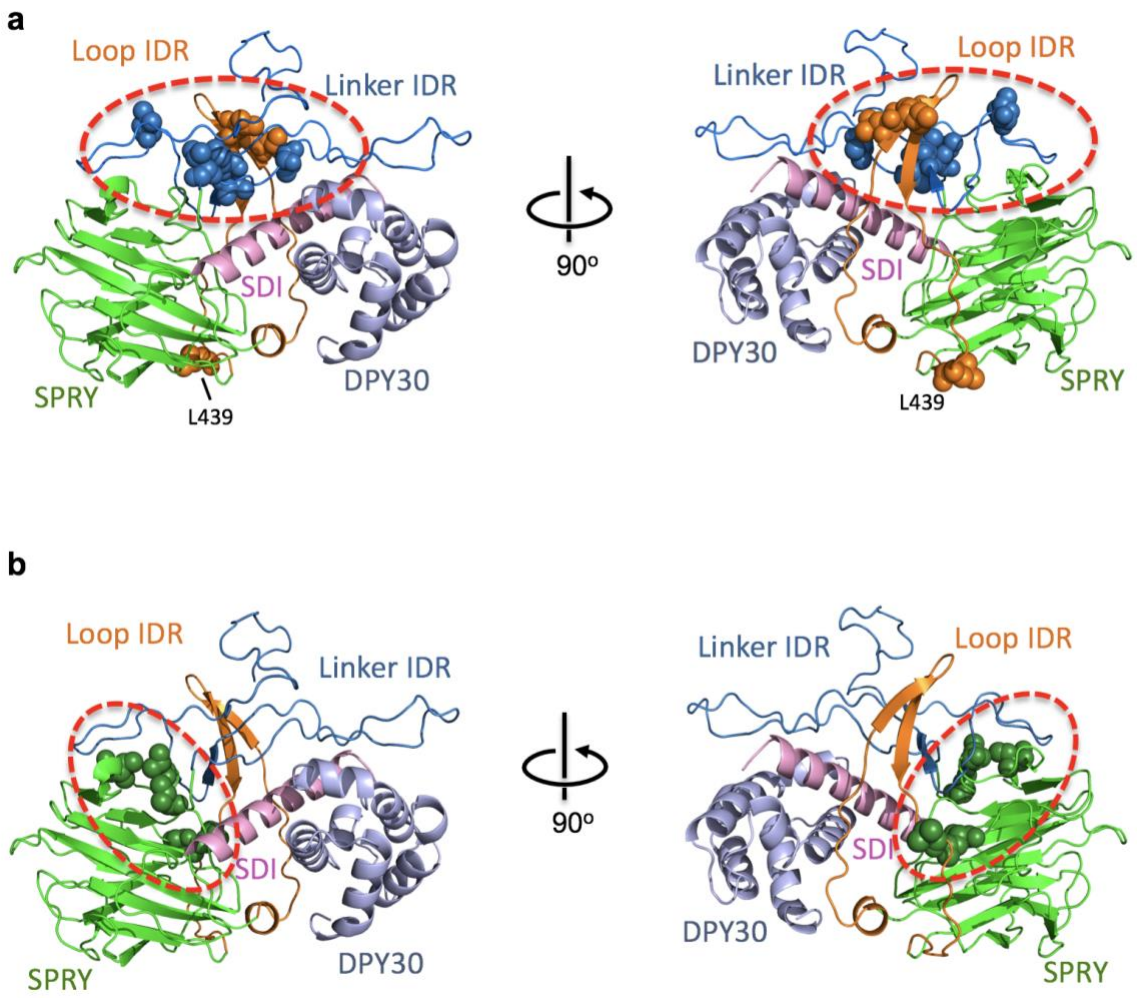

Supplementary Figure 5 | Detailed molecular models that highlight ASH2L IDRs and SPRY regions that undergo DPY30-induced changes in NMR spectra. This figure is related to main Figure 4b. Newly appeared peaks are highlight by sphere representation in the ASH2L-DPY30 structural model. SPRY, green; Linker IDRs, blue; Loop IDRs, orange; SDI, pink. Different viewpoints for **a**, IDR residues and **b**, SPRY residues are shown.

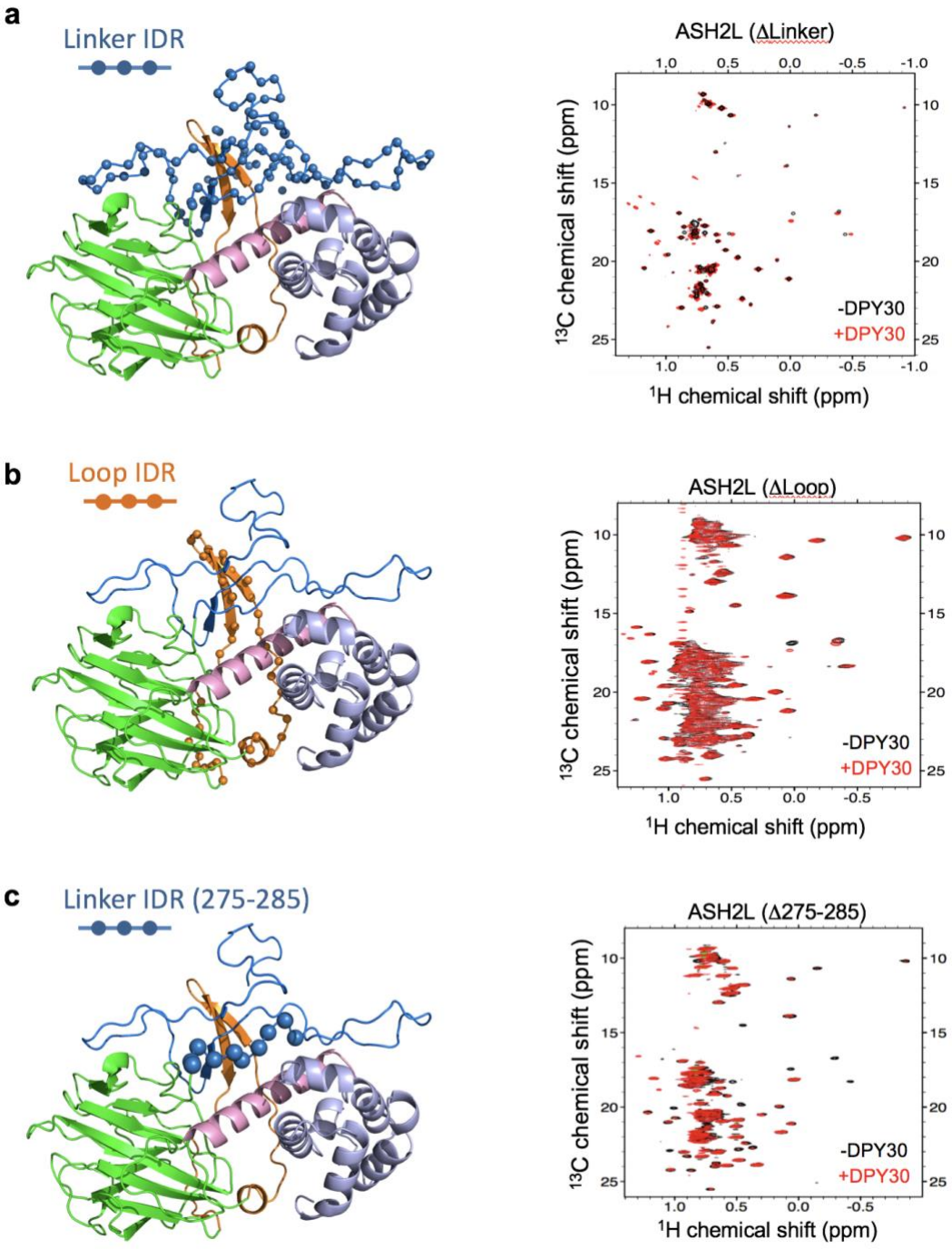

Supplementary Figure 6 | Deletion of ASH2L IDR segments abolished DPY30-induced changes in NMR spectra. This figure is related to main Figure 4. **a-c**, Left, computational models that highlight specific ASH2L IDRs in a spherical representation. **a.** Link IDR; **b.** Loop IDR; **c.** residues 275-285 in Linker IDR. Right, superimposed Methyl-TROSY NMR spectra of [^{2}H, $^{13}CH_3$-ILV] ASH2L$^{202-534}$ with a designated deletion (indicated on top) in absence (black) or presence of homodimeric DPY30 (red). Compared to wild type ASH2L$^{202-534}$, most DPY30-induced changes were abolished in the ASH2L mutants. SPRY, green; Linker IDRs, blue; Loop IDRs, orange; SDI, pink.

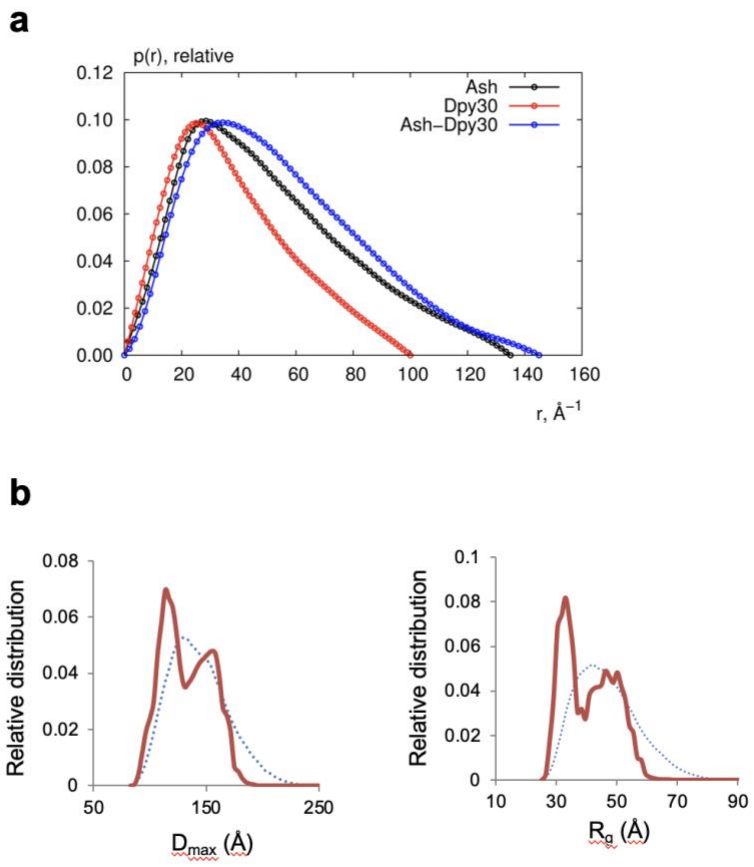

Supplementary Figure 7 | SAXS studies on the free ASH2L, DPY30 and DPY30/ASH2L. This figure is related to main Figure 4. **a,** Pair distance distribution P(r) functions of ASH2L, DPY30 and the ASH2L-DPY30 complex. **b,** Ensemble Optimized Method (EOM) analyses for free ASH2L. Distribution of a pool of 10,000 structures (blue) and optimally fit ensemble (red) are plotted against D_{max} (left) and R_g (right).

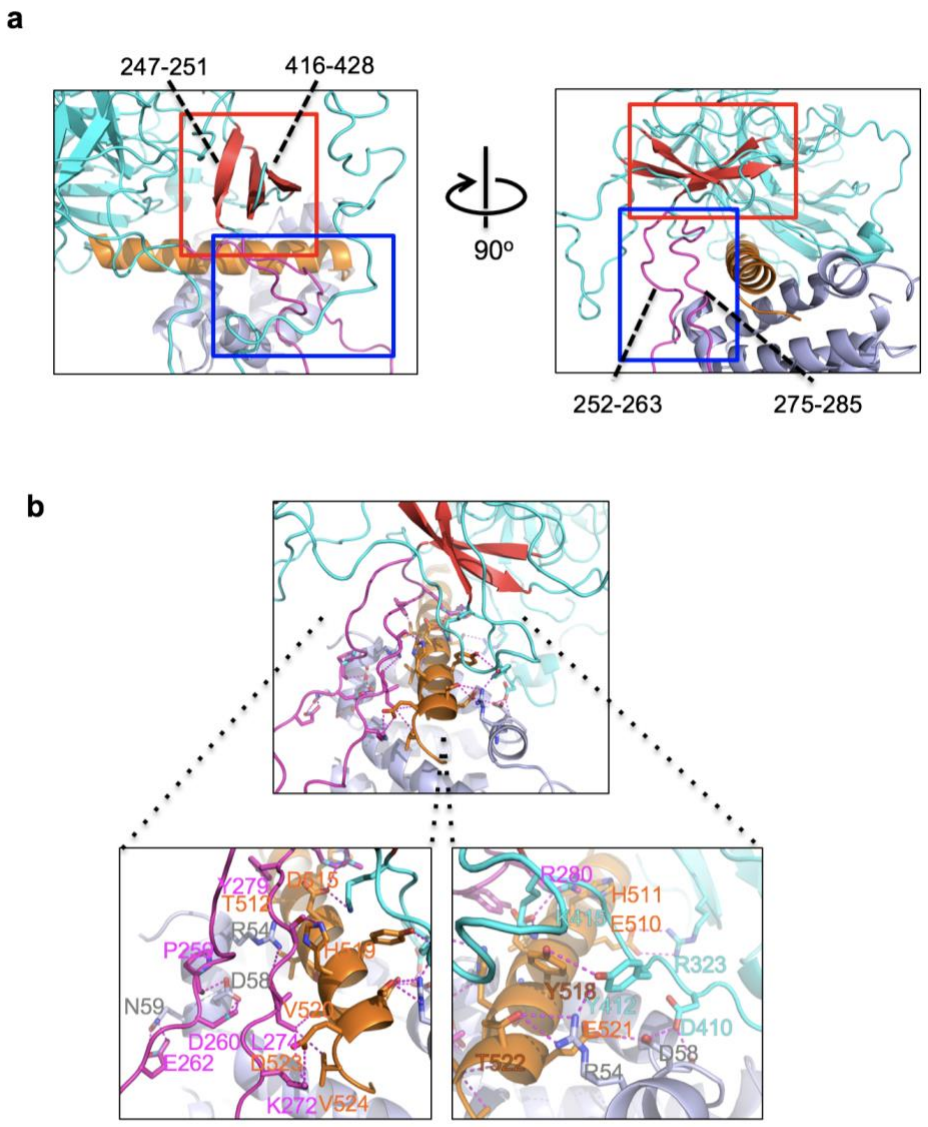

Supplementary Figure 8 | The computational model for ASH2L IDR residues that are important for *in vitro* HMTs activities. This figure is related to main Figure 1-4. **a**, The computational model shows that ASH2L Linker and Loop IDRs likely form a three-strand β-sheet (left) and a β-like structures upon DPY30 interaction. The β-sheet, β-like structure, SPRY domain, SDI of ASH2L as well as DPY30 were labeled in red, pink, cyan, orange and purple, respectively. **b**, The computational model shows likely interactions among residues in ASH2L IDRs and the α-helical ASH2L SDI. The enlarged interaction interface was shown on bottom. Characteristic secondary structures of ASH2L (β-sheet and β-like, α-helical ASH2L SDI) were shown in red, pink and orange, respectively. Residues that make potential direct contacts in the model were highlighted. Notably, some of the highlighted ASH2L residues were tested for MLL1 methyltransferase activity on the NCP in main Figure 1-3.

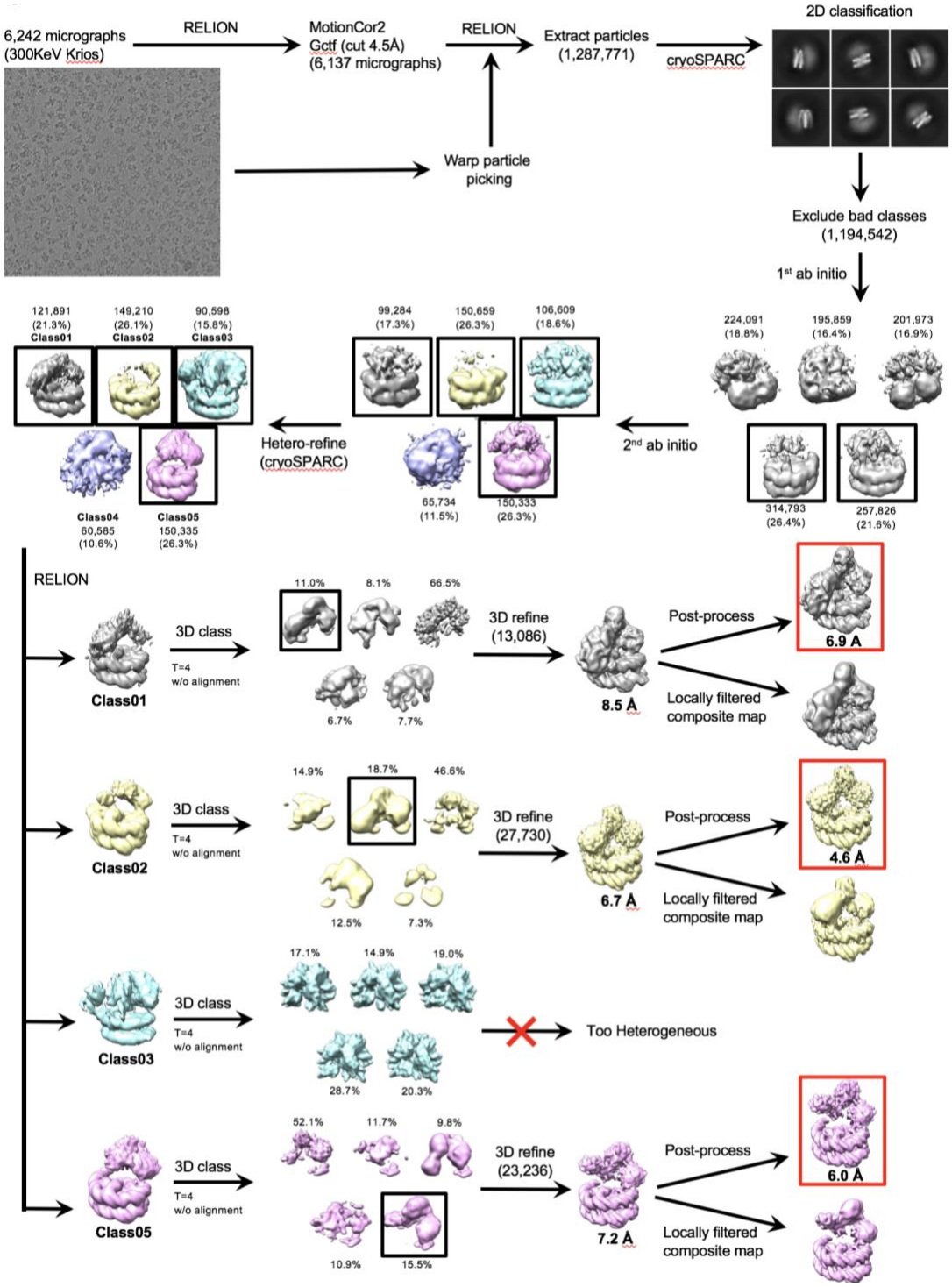

Supplementary Figure 9 | Cryo-EM data processed for 4-MLL1-NCP complex. This figure is related to main Figure 6. Representative micrograph image (Titan Krios 300 KeV) and 2D classifications of the 4-MLL1-NCP complex. The number of particles for each classification and an estimated resolution for overall and selected subcomplexes (red box) were provided. Additional data processing information can be found in the Methods.

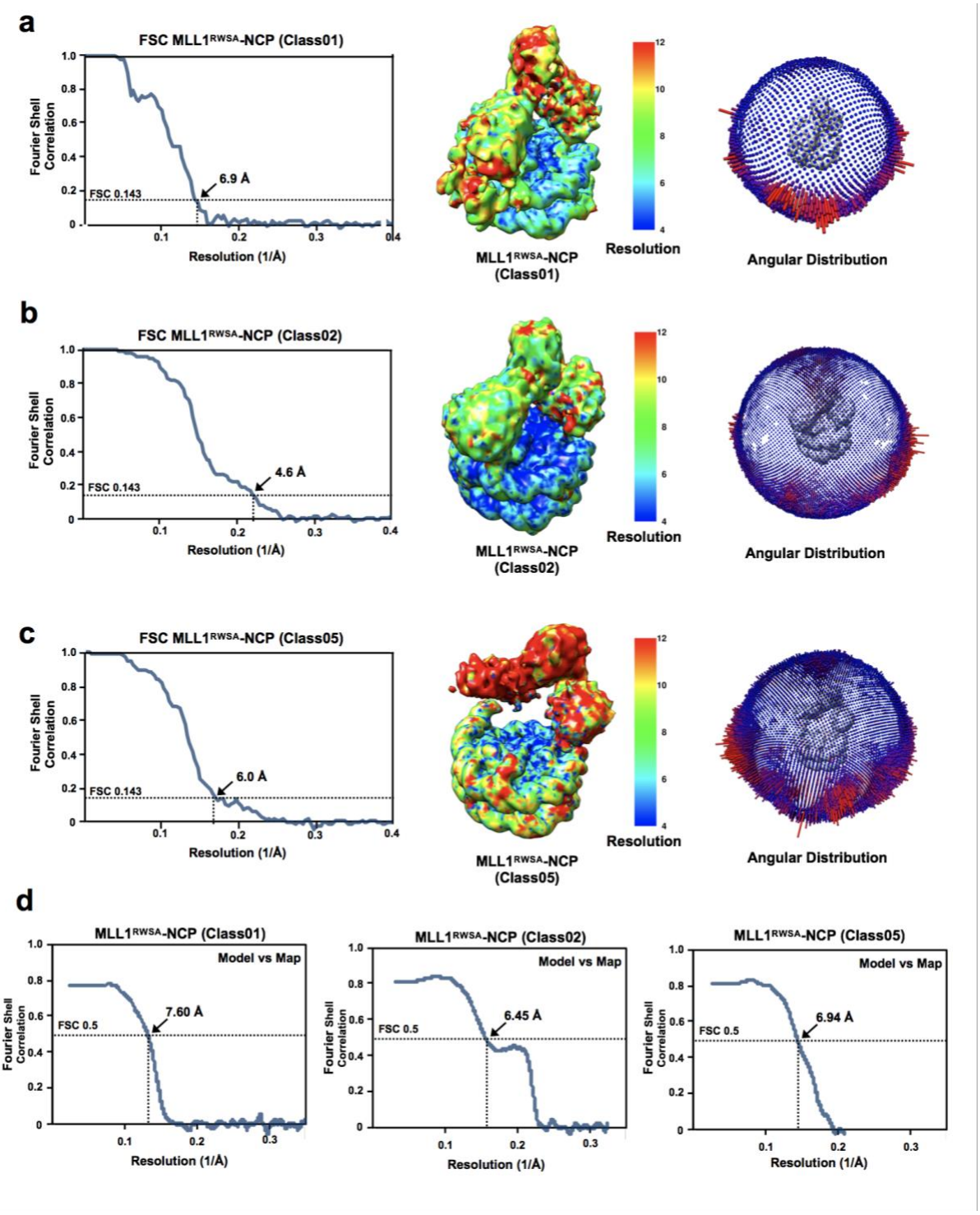

Supplementary Figure 10 | Cryo-EM map validation of 4-MLL1-NCP classifications. This figure is related to main Figure 6. Fourier Shell Correlation (FSC) curves (left), the corresponding local resolution assessment by RESMAP (middle) [2], and angular distribution plots (right) for the 4-MLL1-NCP **a** (Class01), **b** (Class02), and **c** (Class05) particles. The final resolution was determined using FSC = 0.143 criterion, represented by an arrow on each FSC

curve. **d**, Model-map FSC curves for 4-MLL1-NCP Class01, 02 and 05 were calculated using phenix.mtriage [3]. The resolution was found using FSC = 0.5 criterion as indicated by an arrow on each FSC curve.

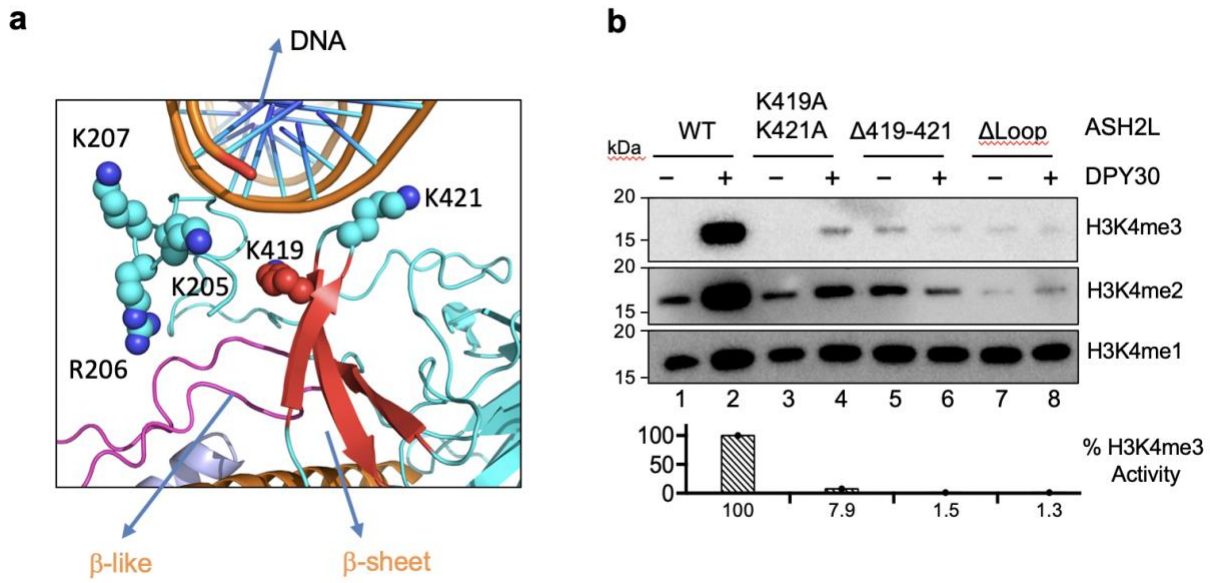

Supplementary Figure 11 | Computational model predicts new contacts between ASH2L IDRs and the NCP. This figure is related to main Figure 5. **a**, Molecular modeling shows that DPY30-induced conformational change in ASH2L IDRs may enable a short loop ($_{419}$-KFK-$_{421}$) in the Loop IDR to interact with nucleosomal DNA. Cryo-EM structure of the 5-MLL-NCP structure (PDB ID: 6PWV and EMDB: EMD-20512) [4] was used for the modeling. Red, DPY30-induced β-sheet structure from ASH2L Linker and Loop IDR; pink, β-like structure from ASH2L Linker IDR; orange, DNA (top). In this model, basic ASH2L residues K419 and K421 are positioned near nuclear DNA. **b**, *In vitro* HMT assay for the MLL1 core complex containing wildtype (WT) or mutant ASH2L proteins as indicated on top. The assays were performed in the presence or absence of DPY30. Antibodies for detection of the methylation products were indicated on right. Mutation or deletion of basic residues in Loop IDR, predicted by the model, drastically reduced MLL1 activity on H3K4me3. Quantification for samples containing DPY30 was performed using ImageJ [1] and presented as relative %activity to that of WT ASH2L.

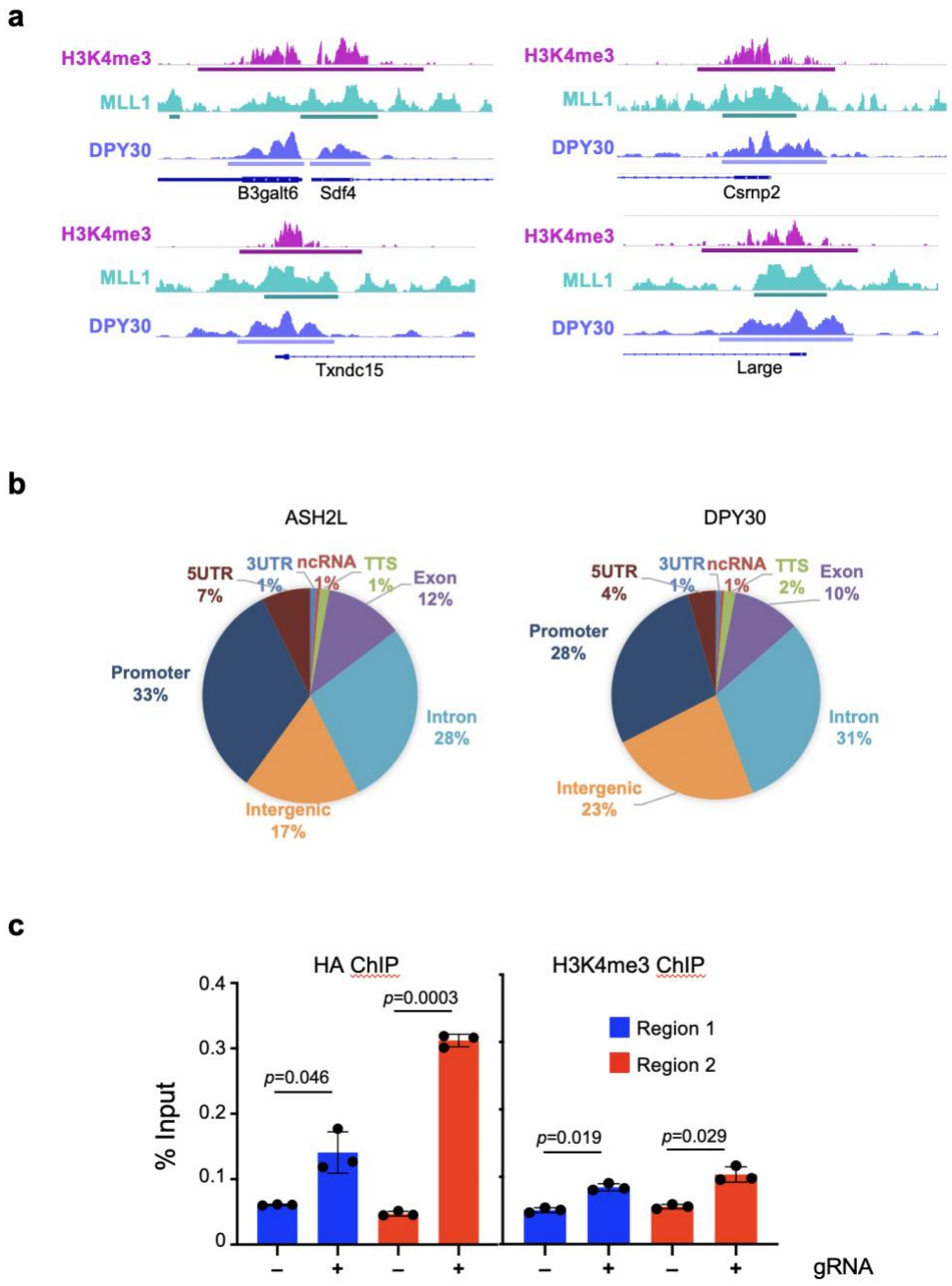

Supplementary Figure 12 | *In vivo* analysis of DPY30 and ASH2L binding and H3K4me3. This figure is related to main Figure 6. **a**, UCSC browser views of H3K4me3, MLL1 and DPY30 tracks at two randomly selected genomic loci. Peaks called by MACS2 were highlighted on bottom. **b**, Pie charts for distribution of ASH2L (left) and DPY30 (right) binding sites relative to annotated gene structures. **c**, The ChIP assay for HA (left) or H3K4me3 (right) in HA-dCas9 cells transfected with or without the pooled gRNAs. This experiment serves as the control for Figure 6b. ChIP signals were normalized against input and presented as %Input. Means and standard

deviations (error bars) from at least three independent experiments were presented. Two-sided student *t* test was performed to calculate *p*-value.

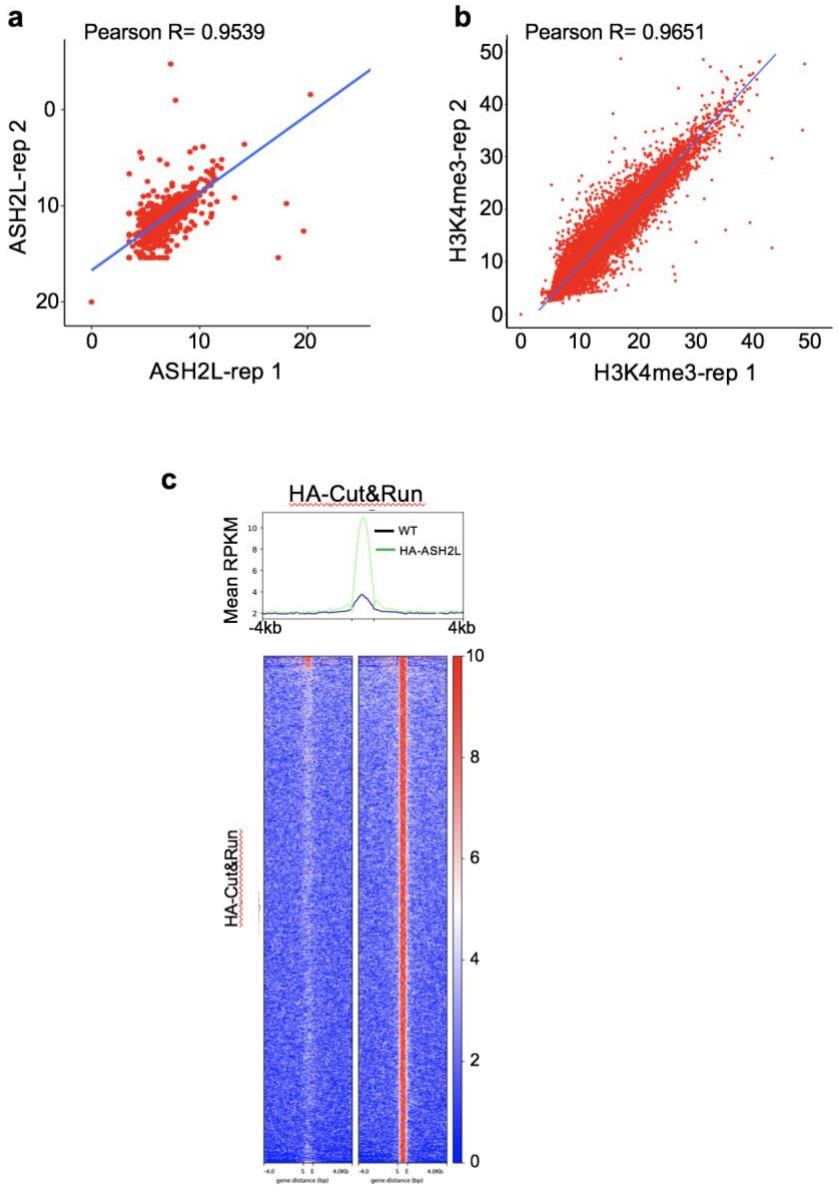

Supplementary Figure 13 | Biological duplicates for ASH2L and H3K4me3 CUT&RUN show good correlation and signal-to-noise ratio. This figure is related to main Figure 6. **a,b**, Scatter plots for peaks in two independent biological replicates of HA (a) or H3K4me3 (b) CUT&RUN. Pearson correlation coefficient for two samples were shown on top. **c**, Heatmap for HA peaks in the control E14 parental cell line and the HA-ASH2L cell line. Merged signals from biological duplicates were shown, with the heat map key at right.

SUPPLEMENTARY TABLES

Supplementary Table 1. Methyl Chemical Shift of ASH2L$^{202-534}$ bound to DPY30. This is related to Figure 4.

Residue	CM1[a]	QM1[a]	CM2[a]	QM2[a]	Residue	CM1[a]	QM1[a]	CM2[a]	QM2[a]
L225	20.459	0.661	21.885	0.75	V391	18.047	1.171	n.d.	n.d.
L231	20.948	0.767	22.188	0.832	L392	19.826	0.163	n.d.	n.d.
L238	19.794	0.947	22.092	0.966	I396	10.303	-0.874		
I250	12.364	0.322			L398	23.874	0.697	n.d.	n.d.
L251	19.437	0.207	24.297	0.489	L408	n.d.	n.d.	n.d.	n.d.
L264	n.d.[b]	n.d.	n.d.	n.d.	L417	21.913	-0.492	22.938	0.03
L266	n.d.	n.d.	n.d.	n.d.	I418	12.245	0.618		
I274	10.333	0.549			L424	21.157	0.297	22.659	0.324
L278	20.459	0.636	23.211	0.845	V432	20.154	0.877	n.d.	n.d.
L283	19.257	0.351	23.385	0.539	L439	19.779	0.54	23.441	-0.238
V287	16.882	-0.355	17.179	-0.049	I447	11.562	0.077		
L288	19.461	1.142	24.123	0.855	I448	10.728	0.485		
L289	n.d.	n.d.	n.d.	n.d.	V454	17.723	0.734	n.d.	n.d.
L291	20.615	0.654	22.66	0.844	V458	18.456	0.79	18.659	0.612
L298	n.d.	n.d.	n.d.	n.d.	I463	10.616	-0.123		
I300	8.308	0.564			V467	n.d.	n.d.	n.d.	n.d.
L305	20.588	1.238	22.974	0.938	I472	12.475	0.57		
V307	n.d.	n.d.	n.d.	n.d.	L474	n.d.	n.d.	n.d.	n.d.
V308	16.942	0.951	17.776	0.905	V480	n.d.	n.d.	n.d.	n.d.
V316	17.723	0.734	21.441	1.012	I482	13.957	0.094		
V322	18.408	-0.545	n.d.	n.d.	L495	20.52	0.316	21.173	0.069
I331	13.053	0.645			V508	19.812	1.213	n.d.	n.d.
V333	n.d.	n.d.	n.d.	n.d.	V509	n.d.	n.d.	n.d.	n.d.
L344	22.929	0.373	23.052	1.032	L513	n.d.	n.d.	n.d.	n.d.
L350	19.329	0.304	23.416	0.378	V516	n.d.	n.d.	n.d.	n.d.
L353	19.284	0.581	n.d.	n.d.	L517	n.d.	n.d.	n.d.	n.d.
L357	n.d.	n.d.	n.d.	n.d.	V520	n.d.	n.d.	n.d.	n.d.
I378	9.422	0.744			V524	19.023	0.822	n.d.	n.d.

[a]Methyl resonances are arbitrarily listed without stereospecific assignment for Leu and Val. For Ile, CM1 and QM1 are equivalent to CD1 and QD1, respectively.
[b]Not determined due to strong ambiguity.

Supplementary Table 2. Cryo-EM Data Collection, Refinement, and Validation Statistics. This is related to Figure 6, S4 and S5.

	4-MLL1-NCP, Class01 (EMD-21542) (PDB: 6W5I)	**4-MLL1-NCP, Class02 (EMD-21543) (PDB: 6W5M)**	**4-MLL1-NCP, Class05 (EMD-21544) (PDB: 6W5N)**
Data Collection and Processing			
Magnification	29,000		
Voltage (kV)	300		
Electron exposure (e-/Å^2)	64		
Defocus range (μm)	-1.5 to -2.5		
Pixel size (Å)	1.00		
Symmetry imposed	C1		
Initial particle images (no.)	1,287,711		
Final particle images (no.)	13,086	27,730	23,236
Map resolution (Å)	6.9	4.6	6.0
FSC threshold	0.143	0.143	0.143
Refinement			
Initial model used (PDB code)	6PWV	6PWV	6PWV
Model resolution (Å)	7.6	6.5	6.9
FSC threshold	0.5	0.5	0.5
Map sharpening *B* factor (Å^2)	-442.70	-177.74	-199.18
Model composition			
Non-hydrogen atoms	19,672	19,574	19,667
Protein residues	1,741	1,729	1,740
Nucleotides	292	292	292
Ligands	-	-	-
***B* factor (Å^2)**			
Protein	214.20	195.04	221.62
Nucleotide	50.98	31.39	51.78
Ligand	-	-	-
Rmsds			
Bond lengths (Å)	0.005	0.005	0.005
Bond angles (°)	0.674	0.673	0.671
Validation			
MolProbity score	2.68	2.59	2.69
Clashscore	44.52	36.36	44.38
Poor rotamers (%)	1.63	1.58	1.63
Ramachandran plot			
Favored (%)	94.21	94.06	94.09
Allowed (%)	5.79	5.94	5.91
Disallowed (%)	0	0	0

Supplementary Table 3. Survey of IDR content in histone methyltransferases. This is related to Figure 2a.

Modification Site	Enzyme	Length (AAs)	IDR (%)
H3R2	CARM1	608	50
	PRMT6	375	12
H3K4	PRDM16	1276	71
	SMYD3	428	0
	MLL1	3969	84
	MLL3	4911	76
H3K9	Suv39H1	412	36
	G9a	1210	66
	SETDB1	1291	38
H3K36	SETD2	2564	90
	NSD2	1365	73
	ASH1L	2969	85
H3K79	Dot1L	1739	82

Supplementary Table 4. gRNA and primer sequence information. This is related to Figure 6c.

gRNAs:

gRNA1-1 sense	CACCGCCCTCTGATCTGTAGCGCAG
gRNA1-1 antisense	AAACCTGCGCTACAGATCAGAGGGC
gRNA1-2 sense	CACCGAGCTGGGTGGTGGACAATGC
gRNA1-2 antisense	AAACGCATTGTCCACCACCCAGCTC
gRNA1-3 sense	CACCGAAGTGCCCAGGGATGATTGA
gRNA1-3 antisense	AAACTCAATCATCCCTGGGCACTTC
gRNA2-1 sense	CACCGTCCTGTGAGGTCCTGCGAAA
gRNA2-1 antisense	AAACTTTCGCAGGACCTCACAGGAC
gRNA2-2 sense	CACCGTGAGGCTAAGGTAATTCAGC
gRNA2-2 antisense	AAACGCTGAATTACCTTAGCCTCAC
gRNA2-3 sense	CACCGCATCTCTGCGTATAGACCAC
gRNA2-3 antisense	AAACGTGGTCTATACGCAGAGATGC

Primers:

CHIP-region 1-F	AGGTCTAACTCAGGCTCCCG
CHIP-region 1-R	ACTGAAGTGACATGTGCGTGTG
CHIP-region 2-F	TGCTGCATTGCCTGTCTTGCT
CHIP-region 2-R	GGTTGCTTACACCTGCCTGTAAC

SUPPLEMENTARY REFERNCES

1. Schneider, C.A., W.S. Rasband, and K.W. Eliceiri, *NIH Image to ImageJ: 25 years of image analysis.* Nat Methods, 2012. **9**(7): p. 671-5.

2. Kucukelbir, A., F.J. Sigworth, and H.D. Tagare, *Quantifying the local resolution of cryo-EM density maps.* Nature Methods, 2014. **11**(1): p. 63-65.

3. Afonine, P.V., et al., *New tools for the analysis and validation of cryo-EM maps and atomic models.* Acta Crystallogr D Struct Biol, 2018. **74**(Pt 9): p. 814-840.

4. Rubin, A.J., et al., *Coupled Single-Cell CRISPR Screening and Epigenomic Profiling Reveals Causal Gene Regulatory Networks.* Cell, 2019. **176**(1-2): p. 361-376 e17.